Check for updates

ADVANCING EARTH AND SPACE SCIENCE

Earth and Space Science

RESEARCH ARTICLE
10.1029/2020EA001229

Special Section:
Jupiter Midway Through the Juno Mission

Residual Study: Testing Jupiter Atmosphere Models Against Juno MWR Observations

Zhimeng Zhang[1], Virgil Adumitroaie[2], Michael Allison[3], John Arballo[2], Sushil Atreya[4], Gordon Bjoraker[3], Scott Bolton[5], Shannon Brown[2], Leigh N. Fletcher[6], Tristan Guillot[7], Samuel Gulkis[2], Amoree Hodges[8], Andrew Ingersoll[1], Michael Janssen[2], Steven Levin[2], Cheng Li[9], Liming Li[10], Jonathan Lunine[11], Sidharth Misra[2], Glenn Orton[2], Fabiano Oyafuso[2], Paul Steffes[8], and Michael H. Wong[12]

[1]Division of Geological and Planetary Sciences, California Institute of Technology, Pasadena, CA, USA, [2]Jet Propulsion Laboratory, California Institute of Technology, Pasadena, CA, USA, [3]Goddard Institute for Space Studies, New York, NY, USA, [4]Department of Climate and Space Sciences and Engineering, University of Michigan, Ann Arbor, MI, USA, [5]Southwest Research Institute, San Antonio, TX, USA, [6]School of Physics and Astronomy, University of Leicester, Leicester, UK, [7]Universite Cote d'Azur, COA, Lagrange CNRS, Nice, France, [8]School of Electrical and Computer Engineering, Georgia Institute of Technology, Atlanta, GA, USA, [9]Astronomy Department, University of California, Berkeley, CA, USA, [10]Department of Physics, University of Houston, Houston, TX, USA, [11]Department of Astronomy, Cornell University, Ithaca, NY, USA, [12]SETI Institute, Mountain View, CA, USA

Key Points:
- Residual analysis provides a direct method to compare any Jupiter atmosphere model with the MWR observations
- The iterative residual analysis process generates 2-D Jupiter maps revealing the deep structures of upper atmosphere features

Correspondence to:
Z. Zhang,
zhimeng@caltech.edu

Citation:
Zhang, Z., Adumitroaie, V., Allison, M., Arballo, J., Atreya, S., Bjoraker, G., et al. (2020). Residual study: Testing Jupiter atmosphere models against Juno MWR observations. *Earth and Space Science*, 7, e2020EA001229. https://doi.org/10.1029/2020EA001229

Received 14 APR 2020
Accepted 18 JUL 2020
Accepted article online 6 AUG 2020

©2020 The Authors.
This is an open access article under the terms of the Creative Commons Attribution License, which permits use, distribution and reproduction in any medium, provided the original work is properly cited.

Abstract The Juno spacecraft provides unique close-up views of Jupiter underneath the synchrotron radiation belts while circling Jupiter in its 53-day orbits. The microwave radiometer (MWR) onboard measures Jupiter thermal radiation at wavelengths between 1.37 and 50 cm, penetrating the atmosphere to a pressure of a few hundred bars and greater. The mission provides the first measurements of Jupiter's deep atmosphere, down to ~250 bars in pressure, constraining the vertical distributions of its kinetic temperature and constituents. As a result, vertical structure models of Jupiter's atmosphere may now be tested by comparison with MWR data. Taking into account the MWR beam patterns and observation geometries, we test several published Jupiter atmospheric models against MWR data. Our residual analysis confirms Li et al.'s (2017, https://doi.org/10.1002/2017GL073159) result that ammonia depletion persists down to 50–60 bars where ground-based Very Large Array was not able to observe. We also present an extension of the study that iteratively improves the input model and generates Jupiter brightness temperature maps which best match the MWR data. A feature of Juno's north-to-south scanning approach is that latitudinal structure is more easily obtained than longitudinal, and the creation of optimum two-dimensional maps is addressed in this approach.

1. Introduction

On 27 August 2016, the Juno spacecraft started its flybys over Jupiter, allowing the microwave radiometer (MWR) instrument (Janssen et al., 2017) to measure the thermal emission of Jupiter's atmosphere from pressure levels of approximately 0.5 bar to a few hundred bars (Bolton et al., 2017). A main objective of the MWR is to measure Jupiter's deep water abundance, because it is key to understanding the history of the giant planet's volatile and heavy elements (Helled & Lunine, 2014) and is essential for understanding the meteorology that is observed at the visible cloud level. Jupiter's brightness temperatures at the MWR wavelengths are highly sensitive to the ammonia distribution in Jupiter's atmosphere (Janssen et al., 2017), the major opacity source in the MWR channels. Prior to the arrival of the Juno spacecraft, the only direct knowledge of Jupiter's deep atmosphere profile (i.e., temperature, water, and ammonia abundances) came from the Galileo Probe, which was restricted to in situ measurements during a single plunge into the atmosphere at a longitude of 4.5°W (System III) and a planetocentric latitude of 6.5°N (within a relatively dry and cloudless area at the southern edge of the north equatorial belt [NEB]) down to less than 20 bars. Most previous works have focused on similarly clear and dry downwelling regions with depletions of ammonia and water, where the probe entered and where spectroscopic measurements are taken (Bjoraker et al., 1986; Grassi et al., 2017). Earth-based radio observations (e.g., de Pater et al. 2016, 2019) give global coverage but require assumptions about limb darkening because viewing angle is correlated with latitude and are limited by the foreground synchrotron radiation emitted by high-energy electrons gyrating around Jupiter's intense

magnetic field (Burke & Franklin, 1955; Santos-Costa et al., 2017). Juno's orbit takes it beneath the radiation belts, largely alleviating the limitations imposed by synchrotron emission and allowing finer spatial resolution than most Earth-based radio observations while observing each location from multiple viewing angles.

Li et al. (2017) have retrieved a vertical ammonia distribution from 0.5 to 100 bars inverted from Juno MWR observations from Juno's first science pass, perijove (PJ) 1, and Li et al. (2020) used MWR data to derive water and ammonia abundance in a narrow latitude band near the equator. de Pater et al. (2019) also derived a vertical ammonia distribution from ground-based Very Large Array (VLA) observations at 3–37 GHz, showing compatibility with a subset of the MWR data described by Li et al. (2017). However, interpreting MWR data in this way requires complex data processing and a variety of assumptions about data smoothness, symmetry of the planet, and so forth (see, e.g., Oyafuso et al., 2020). Instead, in this paper we apply a model in the forward direction to produce synthetic MWR observations and then compare those predictions with the actual MWR data set. This approach is simpler, requires fewer assumptions, and allows direct comparison of residuals with the known uncertainties of the MWR data set (Janssen et al., 2017).

In section 2, we begin with a brief description of the MWR observations. In section 3, we provide details of the modeling approach and present the iterative residual calculation used to generate 2-D Jupiter maps with respect to latitude and longitude. In section 4, we test several Jupiter atmosphere models proposed by previous works against the MWR observations.

2. MWR Observation Description

The Juno/MWR instrument measures the thermal emission of Jupiter's atmosphere at six widely separated wavelengths and multiple emission angles from nadir to greater than 50°. The antenna temperature (T_a) represents the power received by the antenna, which is the convolution of the source brightness temperature (T_b) distribution in the field of view over the broad antenna gain pattern (Janssen et al., 2017), that is,

$$T_a(\theta,\phi) = \int_0^{2\pi}\int_0^{\pi} T_b(\theta'\phi')g(\theta'-\theta,\phi'-\phi)\sin(\theta'-\theta)d\theta' d\phi', \tag{1}$$

where $(\theta'-\theta,\phi'-\phi)$ is the angular deviation from the beam boresight direction (θ,ϕ). $T_b(\theta',\phi')$ is the brightness temperature in the direction of the solid angle element $\sin(\theta'-\theta)d\theta' d\phi'$, and $g(\theta'-\theta,\phi'-\phi)$ is the gain of the antenna toward this direction for an antenna pointed in the direction (θ,ϕ). The gain $g(\theta,\phi)$ (Janssen, 1993, Chapter 1, Equation 1.27) is normalized to 1 over the 4π sky as shown in Equation 2 (Janssen et al., 2017), which makes it a factor of 4π smaller than the commonly defined gain in radio astronomy (Rohlfs & Wilson, 1999, Chapter 5, Equation 5.48).

$$\int_0^{2\pi}\int_0^{\pi} g(\theta,\phi) sin\ \theta d\ \theta d\ \phi = 1. \tag{2}$$

The main beam of the antenna contributes most to the antenna temperature and can be considered as a general estimate of the boresight antenna temperature at (θ,ϕ); however, the sidelobes view a brightness distribution that can be considerably different. For example, we need to account for off-axis Jovian thermal emission at different emission angles, the empty-sky cosmic microwave background, galactic emission, and Jovian synchrotron radiation, the latter being especially significant in Channels 1 and 2.

The gain pattern for each of the six antennas has been measured over the full sphere prelaunch (Janssen et al., 2017) (see Figure 1 for antenna pattern, relative gain with respect to the peak gain). An arbitrary Jupiter atmosphere model can thus be used to calculate the antenna temperature at all positions on Jupiter from all viewing perspectives. This modeled antenna temperature can then be compared with observed antenna temperatures. The residual is defined as the difference between the two:

$$Tresid = T_a^{\text{obs}} - T_a^{\text{model}}. \tag{3}$$

The set of residuals obtained for a given pass is thus a measure of how consistent the model is with the real Jupiter atmosphere. Note also that the radiometric measurements have both systematic calibration uncertainties in addition to thermal measurement noise that must be taken into account, so that interpreting the residuals is not always as simple as minimizing the offset. If the model matched Jupiter exactly, the

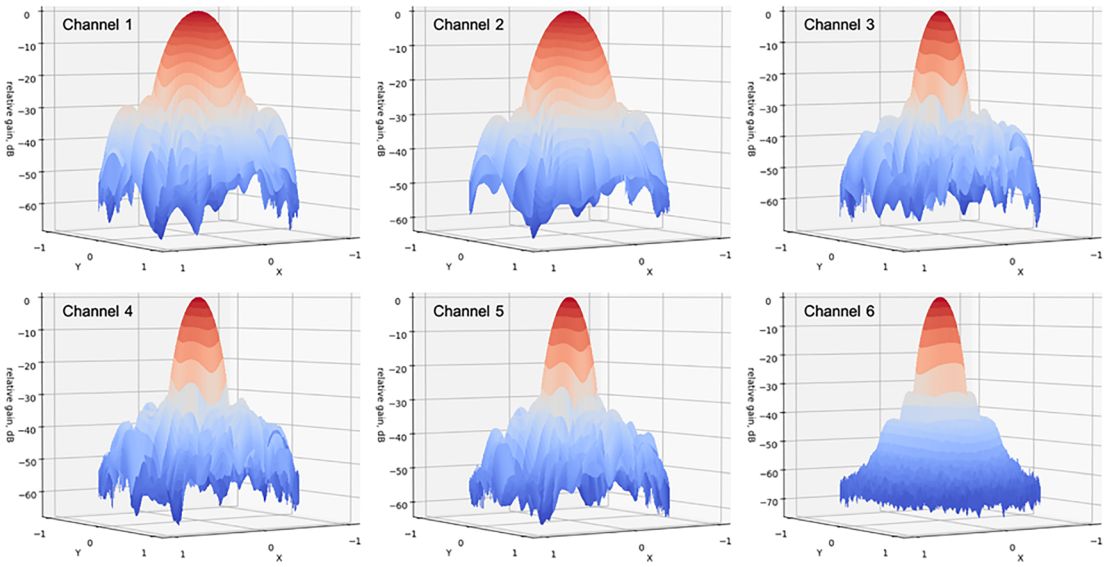

Figure 1. Antenna patterns (relative gain in dB with respect to peak gain) for all six MWR channels. The main beam half power width is 20° for Channels 1 and 2, 12° for Channels 3–5, and 11° for Channel 6. $x = \sin(polar\ angle) * \cos(azimuthal\ angle)$, $y = \sin(polar\ angle) * \sin(azimuthal\ angle)$, where $x = y = 0$ at the boresight.

systematic measurement effect due to absolute calibration error could introduce constant but unknown offsets to all the residuals at each frequency. Janssen et al. (2013) estimate this to be as large as 2%. Other calibration errors such as uncertainties in the measured beam patterns are expected to result in residuals of this order or less (Janssen et al., 2017). Intrinsic receiver noise introduces variations of order 0.1% which leads to scatter in the residuals (Oyafuso et al., 2020). In practice, an atmospheric model would be considered inconsistent with the MWR measurements if the bulk residuals are larger than 2%. It would also be considered inconsistent if the residuals for any channel varied by more than 0.2%.

3. Residual Analysis

We developed a residual analysis method to compare any brightness temperature distribution model over the planet to Juno MWR observations or evaluate any atmosphere profile model to determine if it results in the MWR observed brightness temperatures. We describe and test several published Jupiter atmospheric models against MWR data in section 4. In our analysis, all of the geometries of the spacecraft and the antenna beam coverage are calculated using SPICE kernel information (Acton, 1996). The synchrotron emission and galactic background are accounted for appropriately as described in Oyafuso et al. (2020) and Adumitroaie et al. (2016). In order to verify any proposed atmosphere model with ammonia, water, and temperature profiles, we run the radiative-transfer code JAMRT (Janssen et al. 2013) to simulate the radiative-transfer process and obtain the brightness temperatures at various emission angles and latitudes at all MWR frequencies. For a standard forward model, JAMRT takes in user-specified NH_3 and H_2O enrichment, and an adiabatic temperature profile is then calculated. In a simple standard model, NH_3 and H_2O abundances are uniform in the deep atmosphere and become saturated above the corresponding cloud level. However, JAMRT also allows user-specified NH_3/H_2O abundances and temperature profiles. With six MWR channels sensitive to different pressure levels down to more than 250 bars, the residual values show directly if the composition distribution produced by the atmospheric model is compatible with the data. The effects of ammonia, temperature, and water distributions on brightness temperature are entangled, and deciding whether a specific model is the best one may not be possible using MWR data alone. However, our residual analysis process can determine whether the model is possible in the sense of being consistent with the MWR observations. We calculate the residual value of all observations, each corresponding to an observed emission angle, latitude, and longitude, which indicates how well the proposed model matches the actual Jupiter observations. At any specific latitude, trends in the residual values with respect to the emission

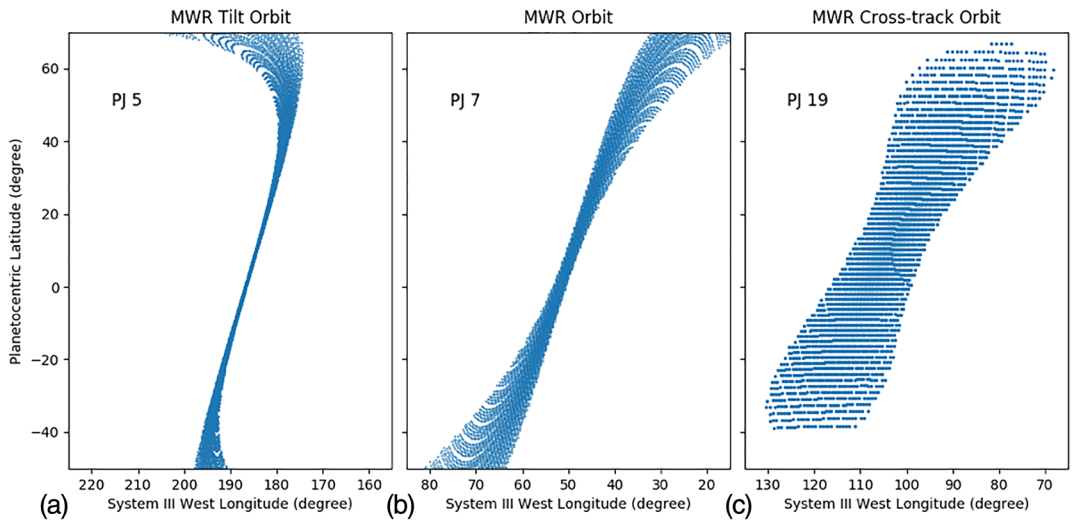

Figure 2. MWR observation tracks for an MWR tilt orbit (a, PJ5 as an example), a typical MWR orbit (b, PJ7 as an example), and an MWR cross-track orbit (c, PJ19 as an example).

angles reveal how well the limb darkening in the proposed model matches the real case. If at large emission angles, the residual values have a downward trend, a larger limb darkening than the proposed value is observed by the MWR observations. We will review test cases in section 4 and explain more about how to interpret the output residual values in terms of Jupiter's atmospheric properties.

Based on the residual analysis described above, we also developed an iterative approach that takes any initial brightness temperature model, calculates the residual values, updates the brightness temperature model based on the residual values, and uses the updated model as a new input brightness temperature in the next iteration. The goal of this process is to converge on a best estimate of Jupiter's brightness distribution along with its emission angle dependence. We iterate the process until the residual values converge and approach zero. This iterative process is a good way to investigate small longitudinal and latitudinal structures and make 2-D brightness temperature maps (with respect to latitude and longitude) of Jupiter at MWR observed pressure levels. At each iteration i, we begin with convolving the regularly gridded input model $Model^i(emissionangle, latitude, longitude)$ with the MWR beam pattern coverage and generate simulated antenna temperatures $T_{a\text{ - model}}{}^i(Obs_{\text{emiss}}, Obs_{\text{lat}}, Obs_{\text{lon}})$ for each observation point. The regularly gridded input model $Model^i(emissionangle, latitude, longitude)$ is in units of brightness temperature at a series of emission angle grids on each Jupiter's latitude-longitude grid. We then subtract the modeled antenna temperature from the observed antenna temperature and derive the output residual values $Residual^i(Obs_{\text{emiss}}, Obs_{\text{lat}}, Obs_{\text{lon}}) = T_{a\text{ - obs}}{}^i(Obs_{\text{emiss}}, Obs_{\text{lat}}, Obs_{\text{lon}}) - T_{a\text{ - model}}{}^i(Obs_{\text{emiss}}, Obs_{\text{lat}}, Obs_{\text{lon}})$, which serve as a proxy for the difference between the input brightness temperature model and the real Jupiter brightness temperature at the corresponding boresight emission angle, latitude, and longitude. We introduce the parameter

$$T^i_{\text{best}}(Obs_{\text{emiss}}, Obs_{\text{lat}}, Obs_{\text{lon}}) = Residual^i(Obs_{\text{emiss}}, Obs_{\text{lat}}, Obs_{\text{lon}}) + T^i_{\text{model}}(Obs_{\text{emiss}}, Obs_{\text{lat}}, Obs_{\text{lon}}), \quad (4)$$

where $T^i_{\text{model}}(Obs_{\text{emiss}}, Obs_{\text{lat}}, Obs_{\text{lon}})$ is the brightness temperature at the observation point according to the input model and $T^i_{\text{best}}(Obs_{\text{emiss}}, Obs_{\text{lat}}, Obs_{\text{lon}})$ is an updated and better estimation for Jupiter's brightness temperature at this specific observing geometry. Constrained by the finite size of our beam and the fact that we lack perfect knowledge of the brightness temperature distribution in adjacent positions at the beginning of this iteration process, $T^i_{\text{best}}(Obs_{\text{emiss}}, Obs_{\text{lat}}, Obs_{\text{lon}})$ will tend to approach the real Jupiter brightness temperature value after each iteration. Several iterations are expected to be needed to achieve a value within measurement uncertainty.

A crucial step in this iteration process is to update the Jupiter model at the end of each iteration. For typical Juno MWR orbits, each latitude was observed at multiple emission angles and within a small longitudinal range (see Figure 2b, as an example of a typical MWR observation track), which is necessary for

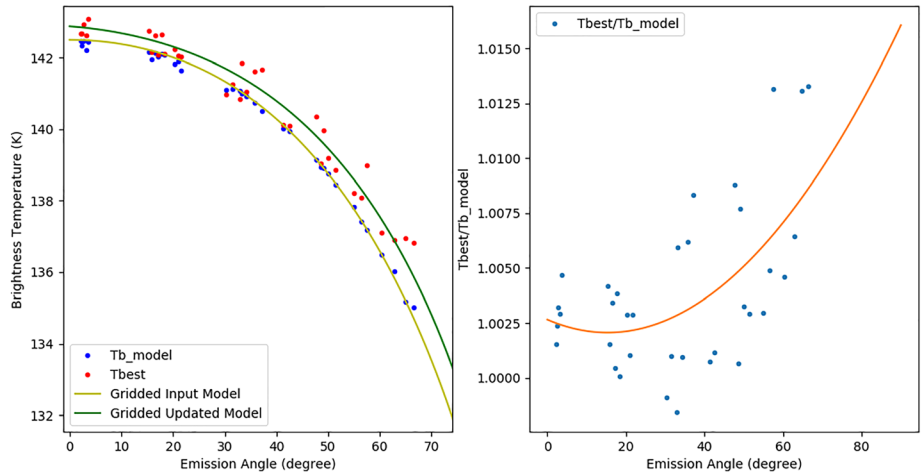

Figure 3. Example of Model-Updating Method 1 at an iteration *i* in one latitude bin of width 0.5°. (left) The yellow curve shows the input gridded model at the beginning of this iteration, and the green curve is the updated model. Blue points show the brightness temperature model for each observation, and red points are the updated brightness at the end of this iteration. (right) The blue points show the value of factor *f* with respect to emission angle, which is then fit with the orange curve, a smooth spline curve function.

determining the limb-darkening value and diminishing the longitudinal variation in each latitude bin. This is accomplished with the spacecraft spin axis orthogonal to its orbital plane and the MWR antenna beams sweeping north to south (antennas fixed to the spacecraft) as the Juno spacecraft also passes over the planet from north to south. A second and special case is the MWR tilt orbit (Figure 2a), which is designed to minimize the longitudinal coverage (the spacecraft attitude is slightly tilted to compensate for Jupiter's rotation) and provide data for more accurate analysis of nadir brightness and limb darkening. For typical MWR orbits, we first ignore the longitudinal variation and derive the best fit brightness model with respect to latitudes and emission angles. After that, with the knowledge of the limb-darkening values, we fix the limb darkening and further derive the best fit nadir brightness temperature model with respect to latitudes and longitudes in order to reveal small longitudinal structures. The cross-track orbit is yet another special MWR orbit (Janssen et al., 2017) (Figure 2c), where at each latitude, a wide range of longitudes are observed but each longitude was only observed once at a specific emission angle. The spacecraft spin axis is parallel with Jupiter's spin axis and the antenna beams sweep from east to west (from lower to higher west longitudes in System III), across the planet as the spacecraft spins. In these cases, at each latitude, the variations due to longitudinal structure and limb darkening are entangled and impossible to distinguish. Therefore, a prior value for the limb darkening at each latitude becomes important. For different data features and also for comparison purposes, we proposed four model-updating methods as described below.

3.1. Method 1: Interpolate and Smooth Among T^i_{best} With Respect to Emission Angles

For typical MWR orbits and MWR tilt orbits with narrow longitudinal coverage, Method 1 is used to derive a brightness temperature model with respect to latitudes and emission angles. The iteration process is not sensitive to the initial model and the residuals converge to near zero usually after five iterations. We assume that at iteration *i*, the input gridded model is $Model^i(emissionangle, latitude)$ covering 90°S to 90°N. In the left panel of Figure 3, blue points show the brightness temperature model $T^i_{\text{model}}(Obs_{\text{emiss}}, Obs_{\text{lat}})$ for each observation point within one latitude bin at the beginning of this iteration, which is based on the input gridded model $Model^i(emissionangle, latitude)$ (yellow curve). At the end of this iteration, we obtain updated brightness temperatures for each observation point $T^i_{\text{best}}(Obs_{\text{emiss}}, Obs_{\text{lat}}) = Residual^i(Obs_{\text{emiss}}, Obs_{\text{lat}}) + T^i_{\text{model}}(Obs_{\text{emiss}}, Obs_{\text{lat}})$ (see red points in left panel of Figure 3). We introduce the factor $f = \frac{T^i_{\text{best}}(Obs_{\text{emiss}}, Obs_{\text{lat}})}{T^i_{\text{model}}(Obs_{\text{emiss}}, Obs_{\text{lat}})}$ (see blue points in right panel of Figure 3). Within each latitude bin, we fit a smooth spline curve function $func(emissionangle)$ to factor f with respect to the emission

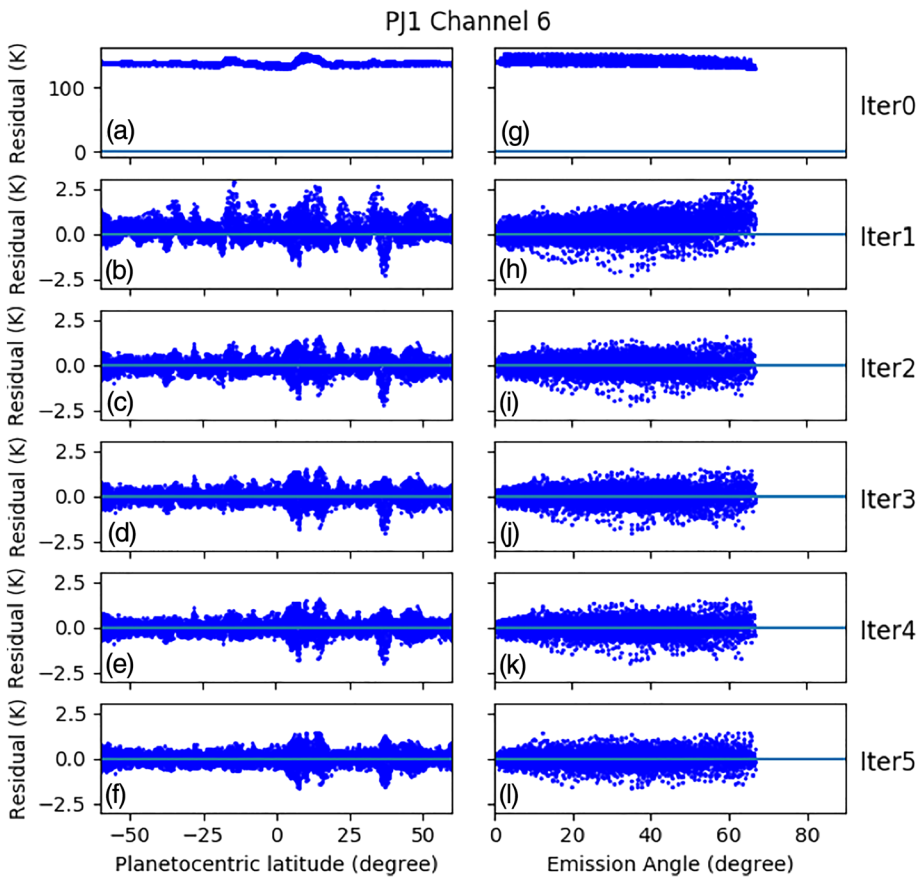

Figure 4. Results from iterative residual analysis on PJ1 Channel 6 observations. (a–f) Residual values with respect to latitude after each iteration, which approach a mean of zero after five iterations. (g–l) The same residual values with respect to emission angle, which becomes flat after five iterations. From the instrument performance model (Janssen et al., 2017), the overall offset of the residuals should be less than 2%, which is ~3 K. In the final iteration, the residuals approach the ~0.3 K instrument noise at most latitudes, with exceptions which we attribute to spatial variations not accounted for in this longitudinally averaged model.

angle (Figure 3, orange curve in right panel) and update the model with $Model^{i+1}(emissionangle, latitude) = Model^{i}(emissionangle, latitude) * func(emissionangle)$. In the left panel of Figure 3, the green curve shows the updated brightness model, which will be used in the next iteration. Thus, we are able to find an updated Jupiter model that catches the main trend in T^{i}_{best} variation against emission angle while minimizing the effect from longitudinal variations.

The iteration process is not sensitive to the initial guess of the brightness model. In Figure 4, we show the iterative results (residual values with respect to latitudes [left column] and emission angles [right column]) for PJ1 Channel 6 through five iterations as an example, starting with a globally uniform 1 K brightness temperature, zero limb-darkening model, which has zero Jupiter brightness information. The right bottom panel in Figure 4 shows the final residual values with respect to emission angle for all latitudes, which reveals how well the limb-darkening value matches the real case. After five iterations, the tilting trend with respect to emission angle is within error bars determined by the instrument performance model. We used Model-Updating Method 1: "Interpolate and smooth among T^{i}_{best} with respect to emission angle" in this test case. Even starting with a model with no real Jupiter brightness temperature information, the residual values approach zero after five iterations, and obvious structures are minimized in the final residual values with respect to latitude or emission angle. Therefore, we can conclude that the final brightness temperature model is a good approximation to the real Jupiter brightness temperature according to MWR observations. It is consistent with observations at the 1-σ level, with all latitudes within expected error bars. Figure 5 shows

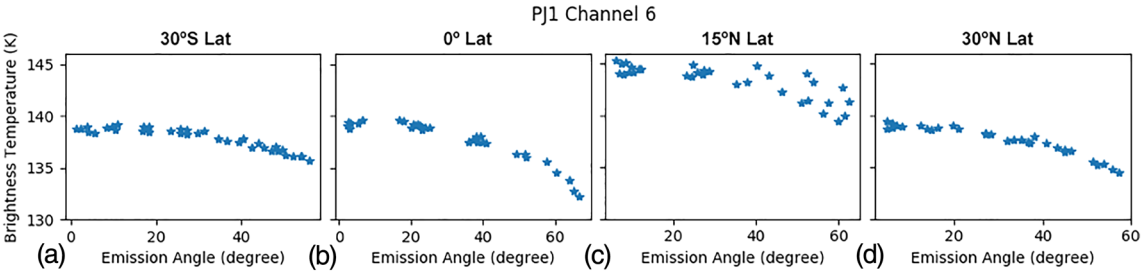

Figure 5. The best-estimated brightness temperature $T_{\text{best}}(Obs_{\text{emiss}}, Obs_{\text{lat}})$ for observations in latitude bins (a) 30°S, (b) 0°, (c) 15°N, and (d) 30°N after five iterations (blue markers), starting with a uniform initial model (1 K at all latitudes and all emission angles).

the final best fit model at four latitudes, where the initial models are 1 K at all latitudes and emission angles. In Figure 4f, we noticed that although the overall offset of the residuals is less than 2% (~3 K) and the residuals approach the ~0.3 K instrument noise at most latitudes after five iterations, at certain latitude bins (such as around 5°N to 20°N and around 35°N), the standard deviation is obviously larger than at other latitudes. This can also be seen in Figure 5 where at 15°N, the brightness temperature versus emission angle curve has more spread. This can be attributed to small longitudinal or temporal structures, which will be dealt with later using model update Method 4—"Fix limb-darkening values."

3.2. Other Model-Updating Methods for Longitudinally Uniform Models

For comparison purposes, we introduced two additional model-updating methods to derive brightness models with respect to latitudes and emission angles.

3.2.1. Method 2: Fit to Three Coefficients

According to theoretical and empirical deduction, the Jupiter limb darkening can be approximated with the three-coefficient equation (Oyafuso et al., 2020):

$$T_B(\theta) = \left[A_0 + A_1(1-\mu) + A_2(1-\mu)^2\right] \cdot f(\theta), \tag{5}$$

where θ is the emission angle and $\mu = cos(\theta)$. A_0 is the nadir brightness temperature, and A_1 and A_2 are the limb-darkening coefficients. $f(\theta)$ is an empirical angular profile suggested by Oyafuso et al. (2020) in order to account for the rapid brightness drop-off at larger emission angles (Figure 2 in Oyafuso et al., 2020). At the end of each iteration and within each latitude bin, this method fits T^i_{best} with respect to μ for all the observations in that latitude bin to the equation above.

3.2.2. Method 3: Spline Interpolation

With this method, T^i_{best} is fitted with respect to emission angle with a spline function. Though MWR also observes Jupiter at high emission angles, due to the large main-beam coverage as projected onto the planet at high emission angles and significant synchrotron leakage into the beam in Channels 1 and 2, we only use observations with emission angles less than 60° ($\mu > 0.5$) to update the Jupiter model. The spline-interpolation method is able to match the brightness temperature variations at these small to medium emission angles but fails to imitate the rapid drop-off at emission angles close to 90°.

In Figure 6, we show examples for updating a brightness temperature model at Channel 6 from Iteration 1 to 2 (with respect to emission angle) at two latitude bins, 70°S and 0°, respectively, using the three different methods described above. The spline-fit results are not able to match the rapid drop of brightness temperature around 90° emission angle, while the three-coefficient fit drops fastest there due to the imposed empirical angular profile.

3.3. Method 4: Fix Limb Darkening

As described earlier in section 3, for typical Juno MWR orbits, each latitude was observed at multiple emission angles and within a small longitudinal range. In these cases, we iterate the process with Model-Update Method 1 to achieve a longitudinal average (considering that the longitudinal range is rather narrow) while varying the limb-darkening profile at all latitudes for each PJ and then apply the limb-darkening profile and iterate with Model-Update Method 4 to obtain the longitudinal variation in nadir brightness temperature.

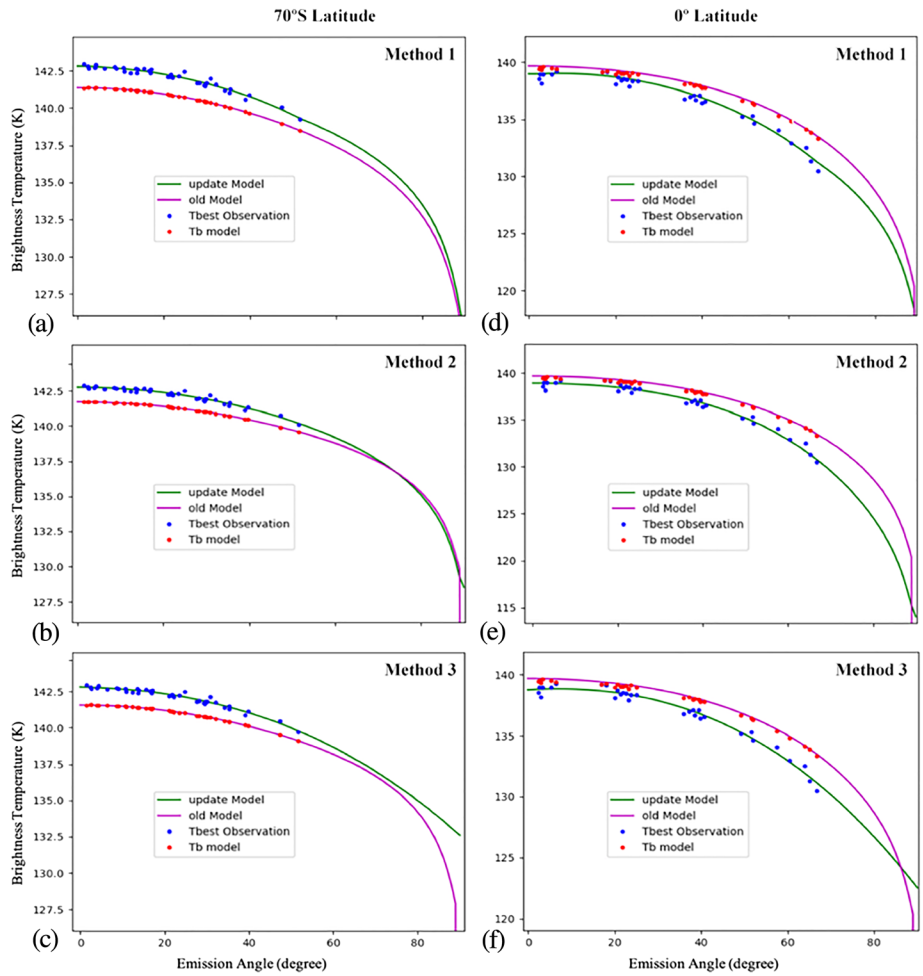

Figure 6. Comparison between three model-updating methods when deriving a brightness temperature model with respect to latitude and emission angle (Channel 6 data as an example). In (a)–(f), red dots show the T^1_{model} derived from input regularly gridded model (magenta curve) at the beginning of Iteration 1, and blue dots show the T^1_{best} which is then used to derive the updated model (green curve) for the next iteration.

We fix the limb-darkening values, and only nadir brightness temperatures at various latitudes and longitudes are updated during these iterations. At the end of each iteration i, T^i_{best} is corrected to the nadir direction by

$$T^i_{\text{best_nadir}}(0, Obs_{\text{lat}}, Obs_{\text{lon}}) = T^i_{\text{best}}(Obs_{\text{emiss}}, Obs_{\text{lat}}, Obs_{\text{lon}}) * \frac{T^i_{\text{model}}(0, Obs_{\text{lat}}, Obs_{\text{lon}})}{T^i_{\text{model}}(Obs_{\text{emiss}}, Obs_{\text{lat}}, Obs_{\text{lon}})}. \quad (6)$$

$T^i_{\text{best_nadir}}(0, Obs_{\text{lat}}, Obs_{\text{lon}})$ is then used to update the Jupiter nadir brightness temperature model on a regular grid. One specific use of this method is to study longitudinal structures and make 2-D (latitude, longitude) Jupiter nadir brightness temperature maps (see Figure 7 as an example for PJ7 Channel 6), which can be compared with visible upper atmosphere features in order to reveal deep structures connected to those features.

As for the special Juno cross-track orbits (such as PJ19), these PJ observations alone are not able to determine longitudinal structures and limb-darkening values at the same time. Therefore, we take averaged limb-darkening values from previous PJs (PJ1 to PJ9) as prior and iterate with Model-Updating Method 4 to make 2-D (latitude, longitude) maps (Bolton et al., 2020).

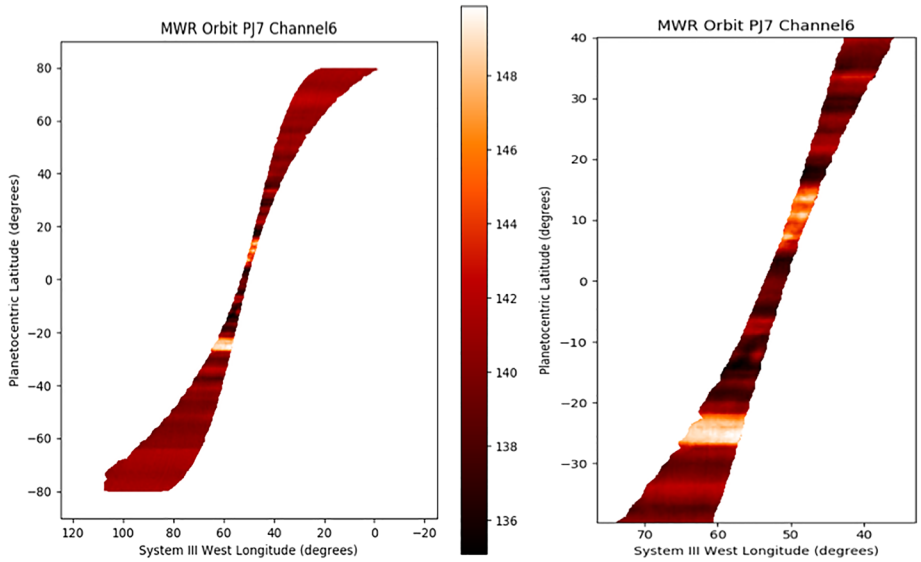

Figure 7. 2-D (latitude, longitude) nadir brightness temperature map for PJ7 Channel 6 obtained after the iterative process with Model-Updating Method 4, which reveals small longitudinal structures, with a blow up map in latitude range 40°S to 40°N on the right.

4. Test Cases—Test Jupiter Atmosphere Models Against MWR Observations

To examine our residual-analysis process and to investigate the science results from it, we test a few previously published ammonia and water concentration profiles against the MWR observations. At microwave frequencies, ammonia, as the main opacity source, affects the brightness temperature most significantly, while on the other hand, the water abundance would affect the atmospheric structure through latent heating and molecular weight effects. The behavior of residuals with respect to latitude and emission angle indicates how well a given profile matches the real Jupiter atmosphere and what modification should be made to better match the observations. Note that the variation in the MWR data due to the instrument noise should be quite small, but none of the models shown here attempt to take into account longitudinal or temporal variations. It is therefore not surprising that the residuals in the following test cases show more variation than instrument noise alone.

The bulk oxygen elemental ratio in Jupiter determines the water abundance in its atmosphere assuming a compositionally homogeneous envelope and is key to discriminating among models for the origin of Jupiter and accretion processes in the planet-forming disk. The water abundance prior to Juno was measured by the Galileo Probe Mass Spectrometer as subsolar down to at least 19 bars (Wong et al., 2004). Wong et al. (2004) reported a mole fraction of H_2O of $(4.1 \pm 1.3) \times 10^{-5}$ at 11.0–11.7 bars and $(4.2 \pm 1.4) \times 10^{-4}$ at 17.6–20.9 bars, which are both averages of data spanning the corresponding pressure range. However, the mixing ratio of H_2O in the deep well-mixed atmosphere was not measured with GMPS and may be higher at deeper levels. Niemann et al. (1998) reported an upper limit to H_2O of 8×10^{-7} at 2.7 bar. More recently, ground-based infrared spectroscopy has constrained water abundance profiles in Great Red Spot spectra as well as typical belt and zone spectra (Bjoraker et al., 2015, 2018). The Great Red Spot spectrum requires a water cloud top at $p \geq 5$ bar, inducing a O/H lower limit of 1.1× solar (corrected to the protosolar O/H ratio of Asplund et al., 2009) (Bjoraker et al., 2018). They also found that the South Equatorial Belt hot spot follows the H_2O profile observed by the Galileo Probe Mass spectrometer and becomes very dry above at $P < 4.5$ bars. The South Tropical Zone has a saturated H_2O profile until reaches its cloud top between 4 and 5 bars (Bjoraker et al., 2018). On the other hand, the water vapor profile retrieved from the Galileo probe Net Flux Radiometer (NFR) measurements (Sromovsky et al., 1998) shows significantly subsaturated water abundance at pressures greater than approximately 1.5 bars. Li et al. (2020) reported on the water abundance in the equatorial region, defined as from 0° to 4° north latitude, to be $2.5^{+2.2}_{-1.5} \times 10^3$ ppm or $2.7^{+2.4}_{-1.6}$ times the protosolar oxygen elemental ratio to H, based on 1.25 to 22 GHz (1.4 to 24 cm) data from Juno MWR probing approximately 0.7 to 30 bars pressure. In Figure 8, we show

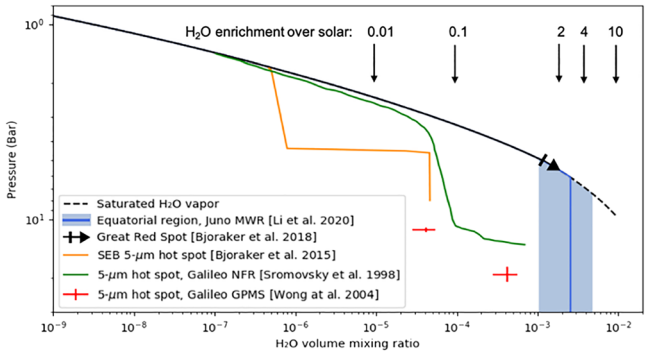

Figure 8. Water abundance distribution profiles in and below the cloud condensation region for different assumed bulk abundances (Bjoraker et al., 2015; Sromovsky et al., 1998; Wong et al., 2004). Blue line with shadowed area shows $2.7^{+2.4}_{-1.6}$ times the protosolar oxygen elemental ratio to H at 0° to 4° North (Li et al., 2020). The black arrow shows the opaque water cloud at $p \geq 5$ bar at Great Red Spot, with a saturated H_2O profile above (Bjoraker et al., 2018). The solar photospheric abundance is according to Asplund et al. (2009), adjusted to protosolar values.

various profiles of H_2O derived from ground-based, Galileo Probe, and Juno data. Arrows denote the water volume mixing ratio corresponding to O/H enrichments ranging from 0.01 to 10 times solar. Ground-based retrievals are shown for a 5 μm Hot Spot in the South Equatorial Belt and for the Great Red Spot, which follows a saturated profile above an opaque cloud at 5 bars. Water abundances derived from two investigations on the Galileo Probe are also shown. The continuous profile is from the NFR; the points with error bars are from the Galileo Probe Mass Spectrometer. Finally, the recent H_2O measurement in the Equatorial Zone by Li et al. (2020) from Juno/MWR is shown in blue along with its error bars in light blue shadowed area. The difference between the derived H_2O abundances from Juno/MWR and Galileo is likely because the 5 μm Hot Spot Galileo probe entered was particularly dry, whereas the MWR measured H_2O in the Equatorial Zone.

Based on Juno/MWR PJ1 nadir brightness temperature data, Li et al. (2017) published an ammonia concentration profile for pressures from 0.5 bar to approximately 200 bars, with a deep ammonia abundance of ~3.5×10^{-4}. Their profile shows a depletion of ammonia over the specified latitude range down to a hundred bars and a column of high-concentration ammonia gas in the northern equatorial zone. We apply their ammonia profile in the latitudinal range from 50°S to 50°N in our residual analysis. As their ammonia profiles are presented in latitude bins of about 2°, a linear interpolation is used for intermediate latitudes. The ideal adiabatic temperature profile (see Figure 9) used by Li et al. (2017) was derived at Equatorial Zone and then applied to all other latitudes. The temperature profile depends on their retrieved deep ammonia and water abundance, with modification in the upper troposphere that are constrained by midinfrared observations (Fletcher et al., 2009). The resulting residual plots are shown in Figure 10 for MWR observations from PJ1 to PJ9 and Channels 1 through 6. The panels on the left show the residuals for their model in the latitudinal direction. Their model is a local model without large-scale circulation. In Channels 4–6, although there are still latitudinal structures in the residuals for individual PJs, when combining all the PJs together, the mean residual values are near zero (excluding PJ7 observations near the Great Red Spot). The variation across PJs in Channels 4–6 suggests unmodeled temporal or longitudinal structures. In Channels 1 through 3, we see deviations around 10°N to 20°N, which shows up in all PJs, suggesting that a different ammonia volume mixing ratio or temperature profile is needed at 10 bar and deeper at those latitudes.

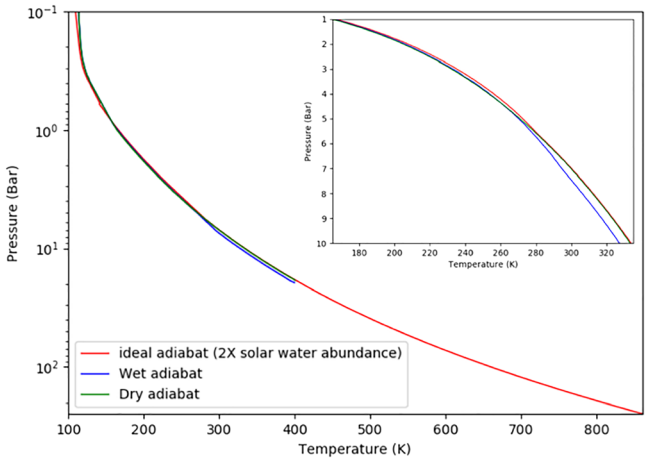

Figure 9. Temperature profiles used in the test cases. (red) Ideal adiabatic temperature profile assuming two solar water abundance in the deep atmosphere. (blue and green) Wet and dry adiabatic temperature profile proposed by de Pater et al. (2019). The inserted figure shows a blowup of these temperature pressure profiles at 1–10 bars in linear scale of pressure.

With the limited knowledge of synchrotron radiation and ammonia/water opacities in the deep atmosphere observed by Channel 1, matching the observations becomes especially difficult. On the other hand, a deviation of temperature from ideal adiabat that Li et al. (2017) assumed is also a possibility. The panels on the right in Figure 10 show how the residuals distribute with respect to emission angles, which is a very important indication for whether the input atmosphere profile generates the correct limb darkening. In Channels 3 to 6, all the distributions are rather flat, and thus, we see no systematic problem with the limb darkening. But in Channels 1 and 2, residuals deviate further from 0 at larger emission angles. There is potential confusion between effects from errors in the temperature profile or from greater synchrotron contribution to the antenna temperature at larger emission angles. However, differences in spacecraft pointing from orbit to orbit would lead to systematic, orbit-dependent trends in the high-emission angle residuals if synchrotron emission was the dominant source of error. Instead, the residuals point to errors at high emission angle that are consistent from

10.1029/2020EA001229

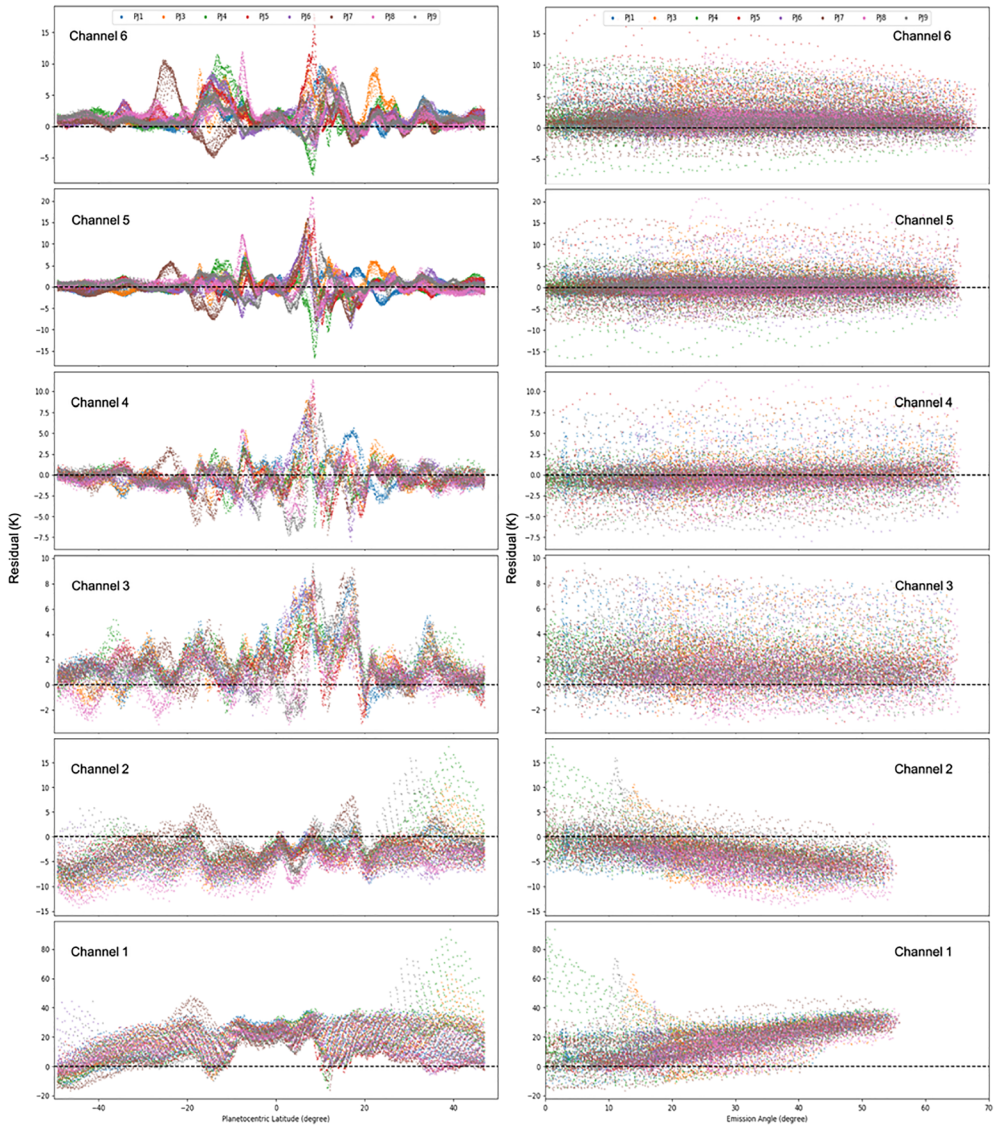

Figure 10. Results for residual analysis on ammonia distribution from Li et al. (2017) using PJ1 to PJ9 observations from Channels 1 to 6. Each perijove is plotted with different colors: blue = PJ1; orange = PJ3; green = PJ4; red = PJ5; purple = PJ6; brown = PJ7; pink = PJ8; gray = PJ9. The panels on left show the residuals of their model in the latitudinal direction; the panels on the right show how the residuals distribute with respect to emission angle.

orbit to orbit. Due to the high residuals at large emission angles, for Channels 1 and 2, Li et al. (2017) focused on data with emission angles smaller than 40°. A more detailed reexamination of the assumptions they made in their model would be helpful in better understanding the MWR data.

Soon after Li et al. (2017), de Pater et al. (2019) analyzed VLA observations between 3 to 37 GHz. Their longitude-smeared spectra show high NH_3 abundance of VMR 4.1×10^{-4} in the deep atmosphere ($P > 8 - 10$ bars), decreasing at higher altitudes (see black line in Figure 13 for their profile at 6.5°N). As shown in Figure 13, the deep ammonia abundance derived by de Pater et al. (2019) and Li et al. (2017) are rather close; however, de Pater et al. (2019) shows ammonia depletion only to 8–10 bars (at most 20 bars at NEB), while Li et al. (2017) showed such depletion much deeper, persisting down to 50–60 bars. The VLA observations were not able to see the atmosphere deeper than 10–20 bars because of strong synchrotron radiation in the foreground at longer wavelength. Both works show a high ammonia concentration in the northern Equatorial Zone (~0–5°N). Another big difference is that Li et al.'s (2017) results show a unique

10.1029/2020EA001229

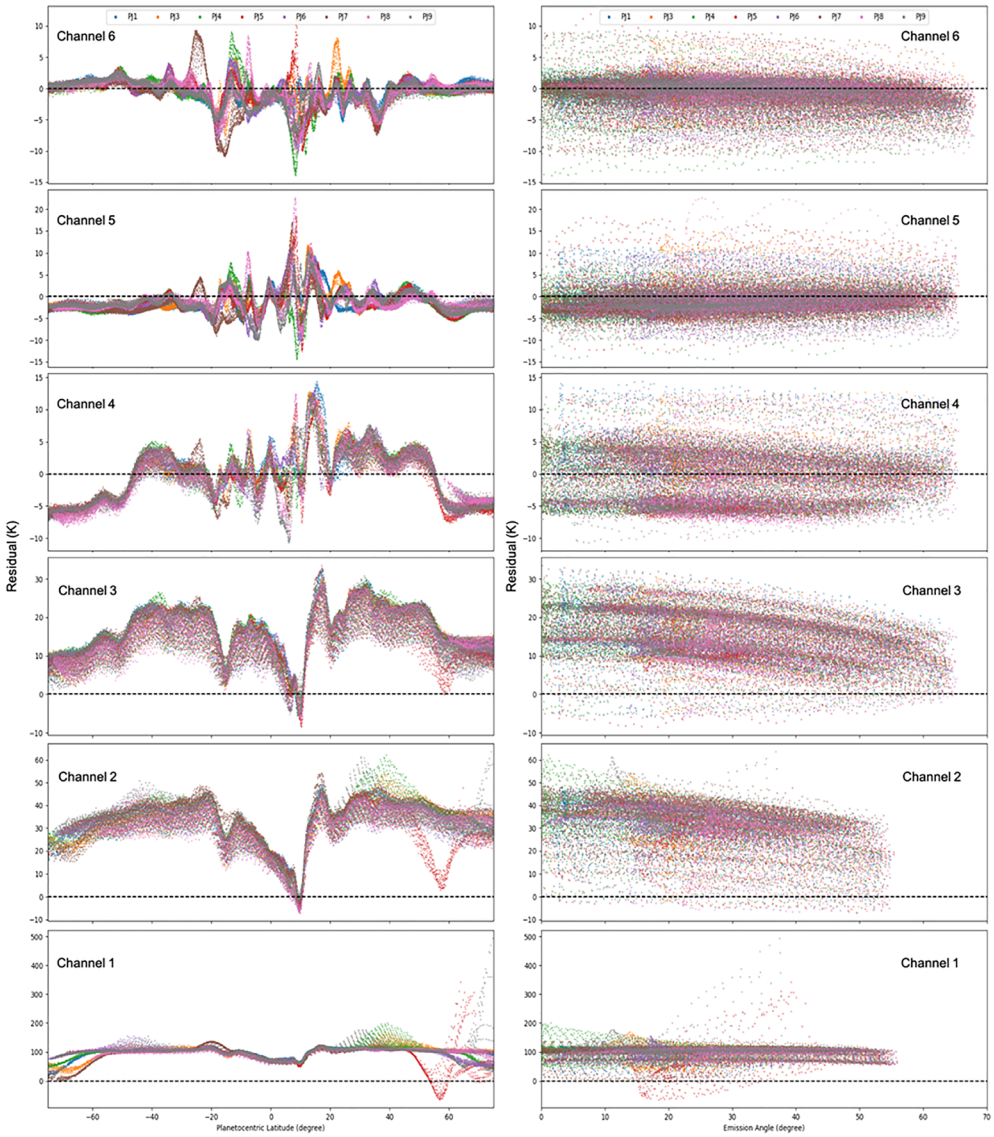

Figure 11. Results for residual analysis on ammonia distribution from de Pater et al. (2019) using PJ1 to PJ9 observations from Channels 1 to 6. The same color code is used as given in the caption for Figure 10. The panels on left show the residuals their model in the latitudinal direction; the panels on the right show how the residuals distribute with respect to emission angle.

ammonia concentration with slight increase with altitudes starting from about 7 to 2 bars and a relatively high abundance just below the NH_3 cloud layer, while the de Pater et al.'s (2019) ammonia concentration profile monotonically decreases with altitude, from well mixed in the deep atmosphere to the ammonia cloud bottom. This pressure range is most sensitive in Juno/MWR Channels 3 through 6. To calculate the residuals of the de Pater et al. (2019) profile in the latitude range from 75°S to 75°N, we employed their dry and wet adiabatic temperature profiles (Figure 9) and 4 times solar water abundance in the deep atmosphere as they proposed (de Pater et al., 2019). As we compared the residual results from the de Pater et al. (2019) model (Figure 11) with the residual results from Li et al. (2017) (Figure 10), in Channels 5 and 6, which is sensitive to $P < 4$ bars and most sensitive around 1–2 bars for Channel 5 and 0.5–0.6 bars for Channel 6, both de Pater et al. (2019) and Li et al. (2017) fit the MWR observations from PJ1 to PJ9 comparatively well at low latitudes. However, in Channel 5, de Pater et al. (2019) starts to deviate from MWR data from middle to high latitudes. In Figure 12, we show the mean and standard deviation of residuals in 2° latitude bins (left column) and 2° emission angle bins (right column) from

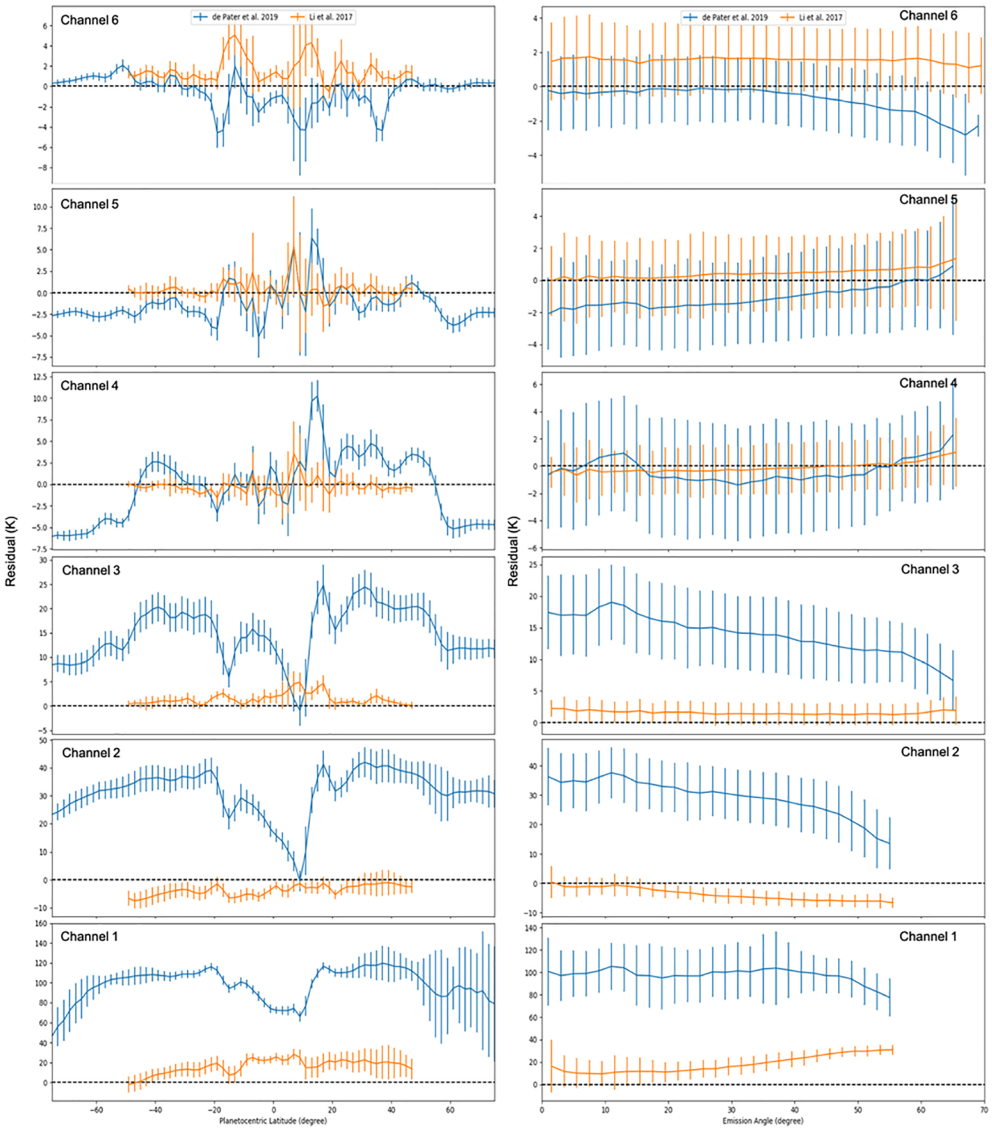

Figure 12. Comparison of mean and standard deviation values of residuals in 2° latitude bins (left column) and 2° emission angle bins (right column) between ammonia distributions from Li et al. (2017) (orange) and de Pater et al. (2019) (blue). The mean latitudes and emission angles in each latitude bin have been shifted 0.5° between the two models in the plot for clearer view.

both Li et al. (2017) (orange curve) and de Pater et al. (2019) (blue curve). The values are derived from residuals in Figure 10 for Li et al. (2017) and in Figure 11 for de Pater et al. (2019) combining all PJ1 to PJ9 results. In Channel 6, at low to middle latitudes, both Li et al. (2017) and de Pater et al. (2019) have mean residuals close to zero, while both miss some small latitudinal structures. In Channel 5, both models match the observations at low latitudes, while de Pater et al. (2019) misses more small latitudinal structures. At middle to high latitudes, Li et al. (2017) matches the observations better than de Pater et al. (2019) in Channel 5. The mean residuals with respect to emission angles are flatter for the Li et al. (2017) model, with an offset less than 1 K for Channels 6 and 5 within the 2% absolute calibration uncertainty. However, there is a downward tilt at large emission angle for de Pater et al. (2019) in Channel 6, suggesting a larger limb darkening is required by the observations. In Channel 4, which is sensitive to $P < 10$ bars and especially around 3–5 bars, both de Pater et al. (2019) and Li et al. (2017) models match the observations from 20°S to 10°N. However, outside this latitude, residuals from de Pater et al. (2019) start to deviate from zero. de Pater et al. (2019) residuals are significantly off zero in

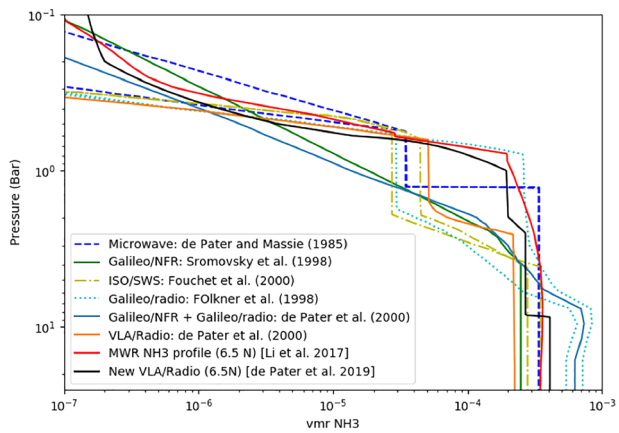

Figure 13. Ammonia abundance distribution profiles from all previous observations around 6.5° N. Except for Li et al. (2017), all other ammonia profiles are considered reaching uniform deep ammonia abundance below ~20 bars.

Channel 3, which is sensitive to $P < 40$ bars and most sensitive around 8–10 bars. For Channels 1 to 3, the residual versus emission angle panel for de Pater et al. (2019) is tilted downward at larger emission angles, suggesting the limb darkening in de Pater et al. (2019) is rather small compared to the real Jupiter atmosphere. At the same time, Li et al. (2017) residuals in Channel 3 still remain around 0, and the limb darkening also matches the data well. As we go deeper into the atmosphere with Channels 1 and 2, Li et al. (2017) residuals are significantly closer to zero as compared to the de Pater et al. (2019) residuals. In Channels 1–3, de Pater et al. (2019) residuals are far above 0, which indicates that the MWR observed brightness temperature is much higher than predicted by their model and could be a sign of too much ammonia concentration in their model at $P > 10$ bars, where VLA (de Pater et al., 2019) were not able to observe.

Before the arrival of the Juno spacecraft at Jupiter, Galileo Probe, which entered at a latitude of 6.5°N (the southern edge of NEB), provided the only knowledge of Jupiter's deep atmosphere profile (i.e., temperature, water, and ammonia abundances below the water cloud base). The Galileo Probe Mass Spectrometer estimated an NH_3 VMR of $5.7 \pm 2.2 \times 10^{-4}$ in the 8.9–11.7 bar region (Wong et al., 2004), and Galileo probe-to-orbiter signal attenuation (Folkner et al., 1998) interpreted with updated ammonia opacities (Hanley et al., 2009) found a maximum NH_3 VMR of $8.4 \pm 0.6 \times 10^{-4}$ at 9.7 bar (with lower NH_3 VMR at both higher and lower pressures along the probe entry path). The NFR inferred a NH_3 VMR of 2.5×10^{-4} at $P \geq 5$ bars, dropping to about 1.5×10^{-4} at 2.5 bars and then decreasing more rapidly with altitudes (Sromovsky et al., 1998). de Pater et al. (2001) presented disk-averaged brightness temperature from VLA observations showing ammonia decreasing at pressure $P \lesssim 4$ bar and a global depletion of ammonia in the region around 2 bars, reaching subsolar ($\lesssim$0.5). All derived ammonia VMR profiles from all of these works are summarized in Figure 13, together with the ammonia concentration profiles of Li et al. (2017) and de Pater et al. (2019) at 6.5°N for comparison. Except for Li et al. (2017) that provides ammonia distribution down to thousands of bars, all other ammonia profiles are considered reaching uniform deep ammonia abundance below ~20 bars. There are a few cases where two lines have the same color and style, indicating estimates of the upper and lower limits: The two blue dashed lines indicate the analysis of microwave data by de Pater and Massie (1985), which show NH_4SH and NH_3 cloud formation at about 1.4 and 0.5 bars with two UV photolysis effect limits in the stratosphere; the yellow dot-dashed lines represent the NH_3 profile inside (lower mixing ratio) and outside (higher mixing ratio) a hot spot from Fouchet et al. (2000) ISO-SWS observations; the cyan dotted lines show the low and high limits from the Galileo probe radio due to the uncertainty in their observations (Folkner et al., 1998). In these test cases, we treat as if these ammonia abundances are globally representative, which is only true in the disk-averaged VLA results (de Pater & Massie, 1985).

We found that the deep ammonia abundance in Li et al. (2017) is very close to the ISO/SWS value outside the hot spot and the disk-averaged VLA results from de Pater and Massie (1985). When calculating the residuals for these profiles, we used the ideal adiabatic temperature profile derived by Li et al. (2017) at Equatorial Zone. For each ammonia profile, we tested a range of possible water-concentration profiles as shown in Figure 8. We show here only the results for a deep water abundance of 2 times solar value. Results for the other water profiles look similar. All of the residuals are plotted in Figures 14a–14f using MWR PJ1 data. Since only the region around 6.5°N is valid for most of these profiles, we have limited the range of latitudes from 0°N to 17°N. For comparison, we also plot the residuals for Li et al. (2017) and de Pater et al. (2019). As we focus at 6.5°N, in the deep atmosphere (Channels 1 and 2), the de Pater and Massie (1985), ISO/SWS, and Li et al. (2017) models fit the MWR antenna temperature best, due to their fairly close deep ammonia abundances. The spread of residuals at one latitude for certain models indicates a limb-darkening mismatch. In Channels 3–5, the disk-averaged VLA results (de Pater & Massie, 1985 and Li et al. (2017) and de Pater et al. (2019) models all result in the smallest residuals at 6.5°N. ISO/SWS residuals start to deviate far from zero at Channel 4 due to their ammonia condensation at relatively high pressures in their abundance profile. In Channel 6, at the troposphere, all models coincide with the MWR observation fairly well except the

10.1029/2020EA001229

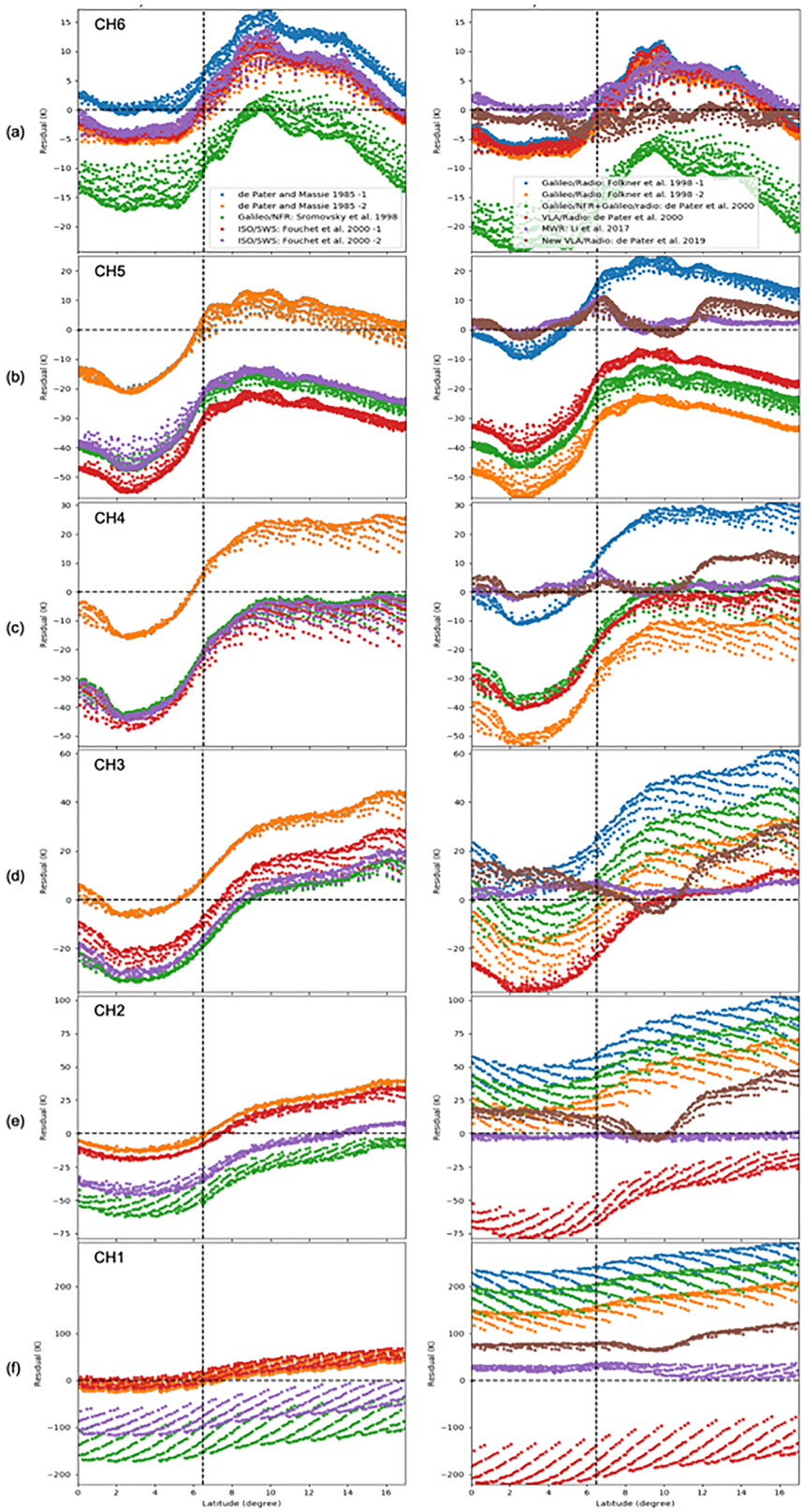

Figure 14. Results for residual analysis on previous published ammonia distributions as listed in Figure 13 using PJ1 observations around 6.5°N from Channels 6 (a) to 1 (f). For each channel, residuals from all 11 models are plotted in two panels for easier viewing.

Galileo Probe NFR result and the disk-averaged VLA (de Pater & Massie, 1985) result with the upper-limit estimate of the effect of UV photolysis on the profile in the stratosphere. Despite the difference in the ammonia profile between disk-averaged VLA (de Pater & Massie, 1985) result with the lower-limit estimate and Li et al. (2017), they are both consistent with the MWR observations at 6.5°N for Channels 1–6. However, due to the finite size of the MWR main beam, a good fit at one single latitude does not guarantee that the model is close to the real Jupiter atmosphere. Even when the MWR beam is centered at 6.5°N, some of the received emission originates at other latitudes.

5. Conclusions

We provide a direct method to compare any Jupiter atmosphere model against the MWR observations through residual analysis. By investigating the residual values at various latitudes, emission angles and channels (sensitive to conditions at pressures between ~1 and 100 bars), we are able to tell which part of the Jupiter model deviates from the observations and often what kind of modification is required. This technique may not provide a unique solution but is useful to identify flaws in existing models. For the two latitudinally resolved models we investigated (Li et al., 2017, and de Pater et al., 2019), they are mostly consistent with MWR observations at low to middle latitudes from Channels 4 to 6, with overall mean residual less or close to the absolute calibration error ~2%. However, our residual analysis from Channels 1 to 3, where ground-based VLA was not able to observe, favors Li et al.'s (2017) ammonia profile with ammonia depletion persisting deeper down to 50–60 bars and with a slightly smaller deep ammonia abundance, while de Pater et al. (2019) overall mean residuals start to be over 4% and reach as high as 12% in Channel 1. Additionally, the iterative process is able to generate Jupiter brightness temperatures with respect to emission angles, latitudes, and longitudes that best match the MWR observed antenna temperatures. The 2-D Jupiter maps with respect to latitude and longitude at all MWR observed pressure levels are of particular interest, as they will be very useful when comparing with upper-atmosphere observations at UV, near-IR, and mid-IR in order to reveal the deep structures of upper atmosphere features (Fletcher et al., 2020).

Data Availability Statement

The Juno MWR observations used in this analysis work are available through the Planetary Data System Atmospheres Node. Data are stored in ASCII tables with supporting documentation (https://pds-atmospheres.nmsu.edu/data_and_services/atmospheres_data/JUNO/microwave.html).

Data files can be found online (https://pds-atmospheres.nmsu.edu/PDS/data/jnomwr_1100/data_calibrated/).

All data sets for this research are available in the citation reference: Zhang, Zhimeng, Adumitroaie, Virgil, Allison, Michael, Arballo, John, Atreya, Sushil, Bjoraker, Gordon, ... Wong, Michael. (2020). Dataset for Residual Study: Testing Jupiter Atmosphere Models Against Juno MWR Observations [Data set]. Zenodo. http://doi.org/10.5281/zenodo.3936065.

Acknowledgments
This work is supported by Juno mission under 699048X.

References

Acton, C. H. (1996). Ancillary data services of NASA's Navigation and Ancillary Information Facility. *Planetary and Space Science*, *44*(1), 65–70. https://doi.org/10.1016/0032-0633(95)00107-7

Adumitroaie, V., Levin, S. M., Costa, D. S., Gulkis, S., & Jansssen, M. A. (2016). Towards a fast background radiation subtraction technique for the Juno mission. *IEEE Aerospace Conference*, 1–11. https://doi.org/10.1109/AERO.2016.7500862

Asplund, M., Grevesse, N., Sauval, A. J., & Scott, P. (2009). The chemical composition of the Sun. *Annual Review of Astronomy and Astrophysics*, *47*(1), 481–522. https://doi.org/10.1146/annurev.astro.46.060407.145222

Bjoraker, G. L., Larson, H. P., & Kunde, V. G. (1986). The abundance and distribution of water vapor in Jupiter's atmosphere. *The Astrophysical Journal*, *311*, 1058–1072. https://doi.org/10.1086/164842

Bjoraker, G. L., Wong, M. H., de Pater, I., & Ádámkovics, M. (2015). Jupiter's deep cloud structure revealed using Keck observations of spectrally resolved line shapes. *The Astrophysical Journal*, *810*(2), 122 (10 pp). https://ui.adsabs.harvard.edu/abs/2015ApJ...810..122B, https://doi.org/10.1088/0004-637X/810/2/122

Bjoraker, G. L., Wong, M. H., de Pater, I., Hewagama, T., Ádámkovics, M., & Orton, G. S. (2018). The gas composition and deep cloud structure of Jupiter's Great Red Spot. *The Astronomical Journal*, *156*(3), 101 (15 pp). https://ui.adsabs.harvard.edu/abs/2018AJ....156..101B, https://doi.org/10.3847/1538-3881/aad186

Bolton, S. J., Levin, S., Wong, M. H., Guillot, T., Kaspi, Y., Arballo, J., et al. (2020). The Depth of Jupiter's Storms.

Bolton, S. J., Lunine, J., Stevenson, D., Connerney, J. E. P., Levin, S., Owen, T. C., et al. (2017). The Juno mission. *Space Science Reviews*, *213*(1-4), 5–37. https://doi.org/10.1007/s11214-017-0429-6

Burke, B. F., & Franklin, K. L. (1955). Observations of a variable radio source associated with the planet Jupiter. *Journal of Geophysical Research*, *60*(2), 213–217. https://doi.org/10.1029/JZ060i002p00213

de Pater, I., Dunn, D., Romani, P., & Zahnle, K. (2001). Reconciling Galileo probe data and ground-based radio observations of ammonia on Jupiter. *Icarus*, *149*, 66–78. https://doi.org/10.1006/icar.2000.6527

de Pater, I., & Massie, S. T. (1985). Models of the millimeter-centimeter spectra of the giant planets. *Icarus*, *62*(1), 143–171. https://doi.org/10.1016/0019-1035(85)90177-0

de Pater, I., Sault, R. J., Butler, B., DeBoer, D., & Wong, M. H. (2016). Peering through Jupiter's clouds with radio spectral imaging. *Science* June, 03, *352*(6290), 1198–1201. https://doi.org/10.1126/science.aaf2210

de Pater, I., Sault, R. J., Wong, M. H., Fletcher, L. N., DeBoer, D., & Butler, B. (2019). Jupiter's ammonia distribution derived from VLA maps at 3–37 GHz. *Icarus*, *322*, 168–191. https://doi.org/10.1016/j.icarus.2018.11.024

Fletcher, L. N., Orton, G. S., Greathouse, T. K., Rogers, J. H., Zhang, Z., Oyafuso, F. A., et al. (2020). Jupiter's equatorial plumes and hot spots: Spectral mapping from Gemini/TEXES and Juno/MWR. *JGR Planets*, *125*(8). https://doi.org/10.1029/2020JE006399

Fletcher, L. N., Orton, G. S., Yanamandra-Fisher, P., Fisher, B. M., Parrish, P. D., & Irwin, P. G. J. (2009). Retrievals of atmospheric variables on the gas giants from ground-based mid-infrared imaging. *Icarus*, *200*(1), 154–175. https://doi.org/10.1016/j.icarus.2008.11.019

Folkner, W. M., Woo, R., & Nandi, S. (1998). Ammonia abundance in Jupiter's atmosphere derived from the attenuation of the Galileo probe's radio signal. *Journal of Geophysical Research*, *103*(E10), 22,847–22,855. https://doi.org/10.1029/98JE01635

Fouchet, T., Lellouch, E., BÅLezard, B., Encrenaz, T., Drossart, P., Feuchtgruber, H., & de Graauw, T. (2000). ISO-SWS observations of Jupiter: Measurement of the ammonia tropospheric profile and of the $^{15}N/^{14}N$ isotopic ratio. *Icarus*, *143*(2), 223–243. https://doi.org/10.1006/icar.1999.6255

Grassi, D., Adriani, A., Mura, A., Dinelli, B. M., Sindoni, G., Turrini, D., et al. (2017). Preliminary results on the composition of Jupiter's troposphere in hot spot regions from the JIRAM/Juno instrument. *Geophysical Research Letters*, *44*, 4615–4624. https://ui.adsabs.harvard.edu/abs/2017GeoRL..44.4615G, https://doi.org/10.1002/2017GL072841

Hanley, T. R., Steffes, P. G., & Karpowicz, B. M. (2009). A new model of the hydrogen and helium-broadened microwave opacity of ammonia based on extensive laboratory measurements. *Icarus*, *202*(1), 316–335. https://doi.org/10.1016/j.icarus.2009.02.002

Helled, R., & Lunine, J. (2014). Measuring Jupiter's water abundance by Juno: The link between interior and formation models. *Monthly Notices of the Royal Astronomical Society*, *441*(3), 2273–2279. https://doi.org/10.1093/mnras/stu516

Janssen, M. A., Ingersoll, A. P., Allison, M. D., Gulkis, S., Laraia, A. L., Baines, K. H., et al. (2013). Saturn's thermal emission at 2.2-cm wavelength as imaged by the Cassini RADAR radiometer. *Icarus*, *226*(1), 522–535. https://doi.org/10.1016/j.icarus.2013.06.008

Janssen, M. A. (1993). *Book: Atmospheric remote sensing by microwave radiometer*. New York, NY: Wiley-Interscience Publication.

Janssen, M. A., Oswald, J. E., Brown, S. T., Gulkis, S., Levin, S. M., Bolton, S. J., et al. (2017). Microwave radiometer for the Juno mission to Jupiter. *Space Science Reviews*, *213*(1–4), 139–185. https://doi.org/10.1007/s11214-017-0349-5

Li, C., Ingersoll, A., Bolton, S., Levin, S., Janssen, M., Atreya, S., et al. (2020). The water abundance in Jupiter's equatorial zone. *Nature Astronomy*, *4*, published February 10. https://doi.org/10.1038/s41550-020-1009-3

Li, C., Ingersoll, A., Janssen, M., Levin, S., Bolton, S., Adumitroaie, V., et al. (2017). The distribution of ammonia on Jupiter from a preliminary inversion of Juno microwave radiometer data. *Geophysical Research Letters*, *44*, 5317–5325. https://doi.org/10.1002/2017GL073159

Oyafuso, F., Levin, S., Orton, G., Brown, S., Adumitroaie, V., Janssen, M., et al. (2020). Angular Dependence and Spatial Distribution of Jupiter's Centimeter-Wave Thermal Emission from Juno's Microwave Radiometer. *Earth and Space Science*.

Niemann, H. B., Atreya, S. K., Carignan, G. R., Donahue, T. M., Haberman, J. A., Harpold, D. N., et al. (1998). The composition of the Jovian atmosphere as determined by the Galileo probe mass spectrometer. *Journal of Geophysical Research: Planets*, *103*(E10), 22,831–22,845. https://doi.org/10.1029/98je01050

Rohlfs, K., & Wilson, T. (1999). *Book: Tools of radio astronomy* (3rd ed.). Berlin Heidelberg: Springer-Verlag.

Santos-Costa, D., Adumitroaie, V., Ingersoll, A., Gulkis, S., Janssen, M. A., Levin, S. M., et al. (2017). First look at Jupiter's synchrotron emission from Juno's perspective. *Geophysical Research Letters*, *44*, 8676–8684. https://ui.adsabs.harvard.edu/abs/2017GeoRL..44.8676S, https://doi.org/10.1002/2017GL072836

Sromovsky, L. A., Collard, A. D., Fry, P. M., Orton, G. S., Lemmon, M. T., Tomasko, M. G., & Freedman, R. S. (1998). Galileo probe measurements of thermal and solar radiation fluxes in the Jovian atmosphere. *Journal of Geophysical Research*, *103*(22), 22,929–22,977. https://doi.org/10.1029/98je01048

Wong, M. H., Mahaffy, P. R., Atreya, S. K., Niemann, H. B., & Owen, T. C. (2004). Updated Galileo probe mass spectrometer measurements of carbon, oxygen, nitrogen, and sulfur on Jupiter. *Icarus*, *171*(1), 153–170. https://doi.org/10.1016/j.icarus.2004.04.010